Imaging corrosion under insulation with a mechanically-translatable atomic magnetometer

1st Benjamin Maddox
Department of Physics and Astronomy
University College London
London, UK
benjamin.maddox.18@ucl.ac.uk

2nd Yuval Cohen
Department of Physics and Astronomy
University College London
London, UK
yuval.cohen.17@ucl.ac.uk

3rd Ferruccio Renzoni
Department of Physics and Astronomy
University College London
London, UK
f.renzoni@ucl.ac.uk

***Abstract*—This work addresses the issue of imaging of corrosion under insulation in pipelines. We demonstrate imaging of recesses of variable depth in an aluminium plate covered by insulation, using a mechanical-translatable atomic magnetometer. This work validates the technology in settings close to real-world scenarios. The technology is of direct impact to the Oil & Gas Industry.**

***Index Terms*—Corrosion under insulation, non-destructive testing, atomic magnetometers**

I. Introduction

The assessment of the corrosion level of pipelines is an important problem in the Oil & Gas Industry. Corrosion Under Insulation (CUI) typically occurs as a localized corrosion damage determined by moisture trapped between the insulation and the pipe to which the insulation is applied [1]–[3]. CUI often leads to catastrophic failure of the equipment, hence its early identification is of paramount importance to the Industry. Access to the pipelines core is made difficult by the presence of insulation, often hard-to-remove asbestos in ageing structures. Current approaches for CUI assessment include infrared thermography, neutron backscattering, radiography, pulsed eddy current testing, and various forms of ultrasonics techniques. Each of these CUI monitoring techniques has drawbacks [3], and efficient large-scale monitoring of CUI in pipelines is still an open problem.

Recent work [4] demonstrated that electromagnetic induction imaging (EMI) with atomic magnetometers (AMs) [5]–[7] can identify and quantify localized thinning of metal plates, thus opening up an alternative viable route for imaging of corrosion under insulation. EMI-AMs is advantageous for CUI imaging with respect to existing techniques: it is simple and low cost, it does not involve ionising radiation, thus being completely harmless, and retains its capability at low frequency, which results in a significant penetrating power both through insulating material as well though the pipeline core structure.

The first proof-of-concept of the use of EMI-AMS towards CUI [4] was realized using a bulky laboratory-based imaging system and moving mechanically a sample with a set of calibrated recesses. Deployment of the technique in real-world scenario requires instead the ability to scan a portable sensor over the fixed target structure. In this work we precisely address this aspect: we progress the technology and demonstrate detection, imaging and characterization of localized thinning of metal plates behind an insulating barrier, mimicking corrosion under insulation, using a mechanically-translatable unshielded atomic magnetometer and a fixed target object, thereby operating close to real-world scenarios.

This work was funded by EPSRC Impact Acceleration Account (grant EP/R511638/1).

II. Experimental set-up

Electromagnetic induction imaging [8], [9] relies on the induction of eddy currents in the target sample, as obtained by the application of an oscillating low-frequency (primary) magnetic fields. The eddy currents will in turn produce a secondary magnetic field. The measurement of the secondary field gives access to the electromagnetic properties of the target, i.e. the conductivity σ, the permittivity ϵ and the magnetic permeability μ. By performing position-resolved measurements it is possible to then produce an image of the object, as a map of its electromagnetic properties.

The use of atomic magnetometers as sensors allows for the operation of the EMI system at low frequency. This is essential for the oscillating magnetic field to penetrate eventual barriers concealing the sample, and increase the penetrating power of the imaging system [10]. This is the set-up used in this work.

A. Imaging system

The imaging system consists of a compact radio-frequency atomic magnetometer (RF-AM) [11], [12] operating in electromagnetic induction imaging modality [13], [14]. The system was described in detail previously [15], [16], and we recall here only the essential details.

The sensor head is shown in Fig. 1 and consists of a mechanically-translatable RF-AM weighing 1.49 kg with dimensions $110 \times 110 \times 145$ mm^3 (W $\times$ L $\times$ H). All the optical and electronic components are held in place by a support in nylon, 3D printed via selective laser sintering (SLS). The sensor head is enclosed by a cover printed in the same material. A cubic glass cell ($20 \times 20 \times 20$ mm^3) containing isotopically enhanced ^{87}Rb vapour and 20 Torr of N_2 buffer gas sits at the centre of the sensor head. Two Vertical Cavity

Surface-Emitting Lasers (VCSELs), with internal thermoelectric coolers and thermistors, generate the circularly polarised pump beam for the preparation of the atomic sample and the probe beam for its interrogation. The magnetic bias field required to tune the magnetometer is generated and stabilised by three pairs of orthogonal Helmholtz coils centred on the cell. A 3-axis fluxgate sensor (Bartington MAG612) close to the cell acts as the feedback to three servo controllers which actively adjust the current in each coil. The sensor head also includes a polarimeter, and an RF coil used both to drive the atomic precession and to induce eddy currents in the sample of interest. The sensor is moved using a motorised 2D mechanical translational stage, so to interrogate different points of the target object.

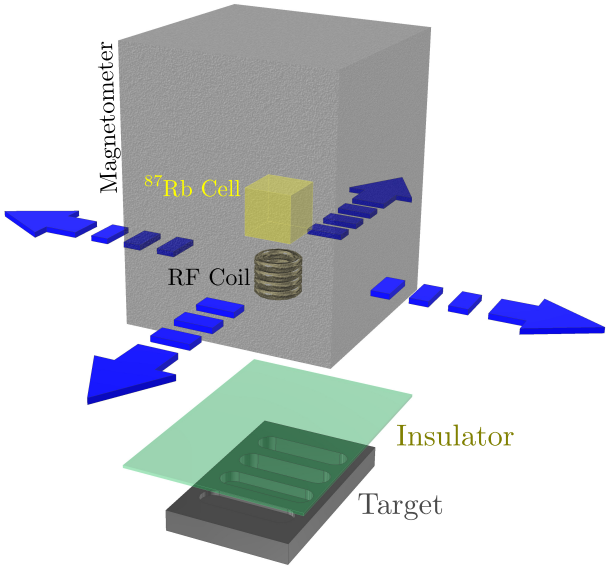

Fig. 1. Sketch of the experimental set-up. The sensor head includes the rubidum vapor cell, the rf coil used to drive the atomic spin precession and to induce eddy currents in the target object, the two laser sources with the related optics, the polarimeter used to interrogate the probe beam polarization, the coil assembly for the generation and stabilisation of the bias magnetic field, and the compensation of spurious low-frequency fields. The sensor head can be moved on a plane using a motorised 2D mechanical translational stage.

The sensor head is connected via flexible electrical cables to a control unit, which includes the following equipment: two current controllers and two temperature controllers for the operation of the two VCSEL lasers, power supplies and proportional-integral-derivative (PID) controllers for the three-axis coils used to set and stabilise the bias field, and a lock-in amplifier which drives the RF coil and reads out the polarimeter output.

B. Procedure

The spin precession driven by the total RF field, as determined by the sum of the applied RF field and the field produced by the eddy currents induced in the target object, is read out by monitoring the Faraday rotation of the plane of polarization of the probe beam produced by the interaction with the atomic vapour. The polarization of the probe is interrogated by a miniaturized polarimeter, included in the sensor head, and processed with a lock-in amplifier (LIA), providing phase-sensitive detection of the magnetic resonance which carries information of the target properties. The position of the maximum of the resonance is determined by fitting it with a Lorentzian, and the amplitude R and phase output ϕ of the LIA are read out for a finite frequency offset from the maximum. Taking measurements at a finite frequency offset has proved to minimise phase noise while scanning over the sample, and results in a higher quality of the imaging [17], [18].

C. Samples

Corrosion of a metallic structure results in its thinning. A deeper corrosion damage corresponds to a more pronounced thinning of the structure. In the present work representative samples are produced by cutting recesses of different depth in an aluminium plate, thus simulating different levels of corrosion. Four slots with incremental recess depths 3 mm, 6 mm, 9 mm, then a through-cut slot at 12 mm (to compare to a hole) were cut on the plate, as shown in Fig. 2.

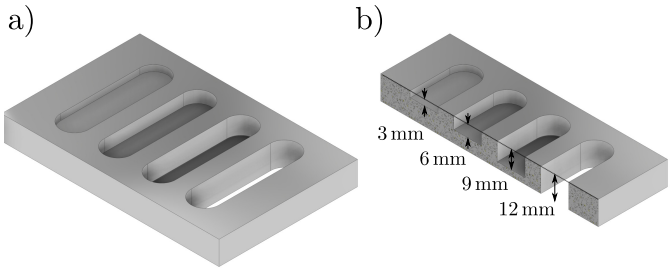

Fig. 2. Sample used for the proof-of-concept of imaging of corrosion under insulation. The plate is in aluminium with size 110 mm × 70 mm × 12 mm. The recesses correspond to 25%, 50%, 75% and 100% (through-cut hole) of the plate depth.

III. Results

Electromagnetic induction imaging was performed by translating the atomic magnetometer over the sample, which is placed with the recesses facing the magnetometer as in Fig. 1, and recording for each position the R and ϕ response at a fixed frequency detuning from the maximum of the atomic resonance.

Typical results in the absence of insulation are shown in Fig. 3, with panel (b) and (c) displaying a spatial map of R and ϕ, respectively. The images reveal each slot as a variation in R and ϕ. Additionally, the amplitude of the response in R and ϕ depends on the slot depth. This gives access to the depth of the recess, and allows one to assess the corrosion level in a structure.

Data as in Fig. 3 allows for the determination of the centres of the recesses, and for the quantification of their depth. The analysis proceed as follows. We define a portion of the plate by introducing two boundaries parallel to the y axis; these

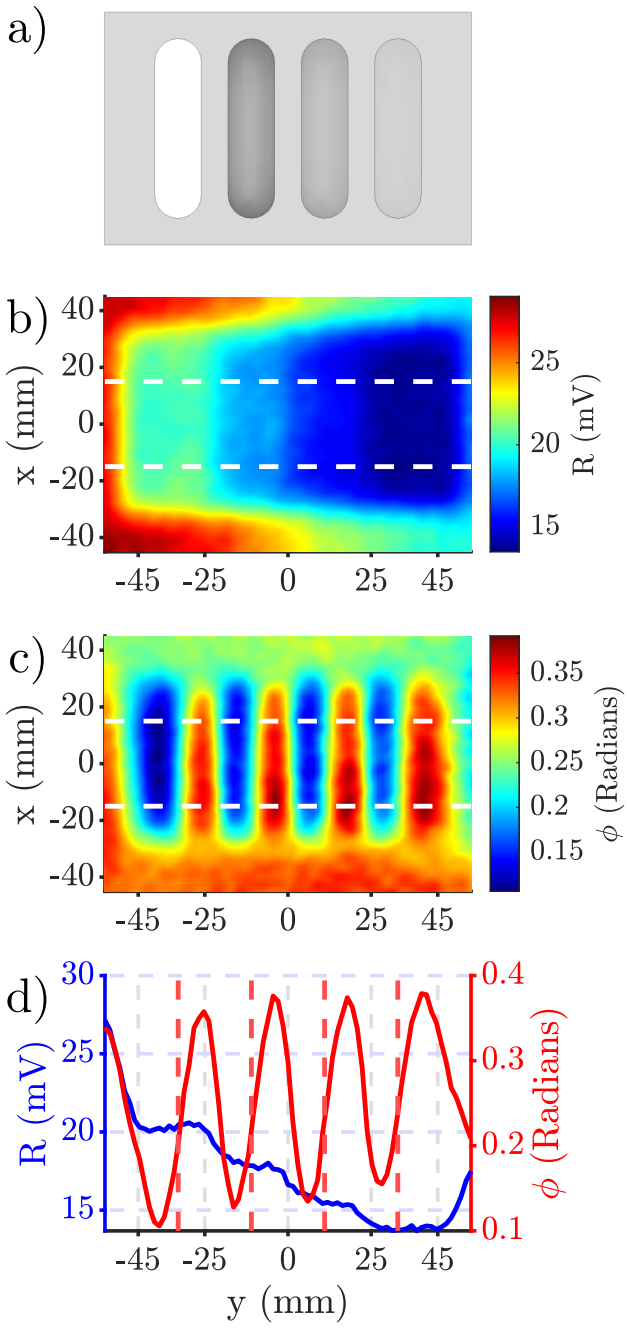

Fig. 3. Experimental results for electromagnetic induction imaging of the sample plate which includes three recesses of variable depth and a cut-through hole. Panel (a) reports the drawing of the sample plates with the recesses, so to visually guide the interpretation of the other panels. Panels (b) and (c) reports the R and ϕ map, respectively, obtained via electromagnetic induction imaging. The horizontal lines in the second and third panels indicate the boundaries of the region of interest, which excludes the boundaries of the recesses in the extreme x positions. These boundaries are to show the range of measurement points used to generate data for panel (d). Panel (d) shows the spatial variation of R and ϕ along y, after averaging along x within the boundaries defined by the white dashed lines. The imaging was done at 55 kHz and the resolution of the translational stage was 1.5 mm. The images are filtered with a gaussian filter with a radius of 1 pixel. The vertical lines in panel (d) show the position of the centres of the slots, as determined by the procedure described in the main text.

boundaries are represented by dashed lines in Fig. 3(b,c). The boundaries are chosen so that the edges of the recesses, corresponding to the extreme x values, are located outside the portion of the plate defined by the boundaries, and will not be included in the data analysis. The data included within the region of interest bounded by the dashed lines of the maps of Fig. 3(b,c) was used to determine the position of the centres of the recesses.

For a given value of y, the measurements for ϕ (and then for R) for the different x positions within the region of interest defined by the white lines were averaged to produce a single value of ϕ (and then for R). Then the obtained data for the average ϕ and R for different values of y were interpolated as a function of y, with results shown in Fig. 3(d). We use a simple peak detection algorithm in MATLAB to define the peak and trough. We then define the recess centre as the midpoint between the peak and trough of the dispersive shape in ϕ, as in our previous work on pilot-hole detection [16].

An additional series of measurements were taken by introducing a 1.5 mm thick insulating layer between the aluminium plate and the sensor head, with results as in Fig. 4. Also in this case, the recesses were clearly identified in the maps obtained via EMI and the response was found to depend on the depth of the slot, therefore demonstrating the potential of the technique to assess and image corrosion under insulation.

More quantitative conclusions about the ability of discriminating between recesses of different amplitude can be obtained by determining from the data the signal amplitude at the center of the different recesses. We determine the recess center by taking the midpoint between the peak and trough of the ϕ trace, as previously discussed. The interpolated value R of the LIA output amplitude at the recess center is then plotted in Fig. 5 for the different recesses, both for the case of a bare plate and for the case of an insulated sample. In both cases the signal amplitude R was found to depend linearly on the depth recess, thus confirming the ability to discriminate between recess depth by measuring the electromagnetic response. We notice that Fig. 5 evidences a different linear dependence for R vs the recess depth depending on the presence or absence of insulation. We attribute this difference to the effective lift-off introduced by the insulating layer.

IV. Conclusions

This work progresses the technology towards imaging of corrosion under insulation using an atomic magnetometers. It specifically demonstrates identification, imaging and characterization of recesses in an aluminium plate using a translatable atomic magnetometer operating in induction imaging modality. The recesses mimic thinning due to corrosion. We demonstrated that the imaging response depends on the depth of the recess, also in the presence of an insulating layer. This validates the technology in settings close to real-world scenarios.

The ability to tune the penetration depth of the imaging by varying the frequency of the oscillating magnetic field could provide an important handle toward full tomographic

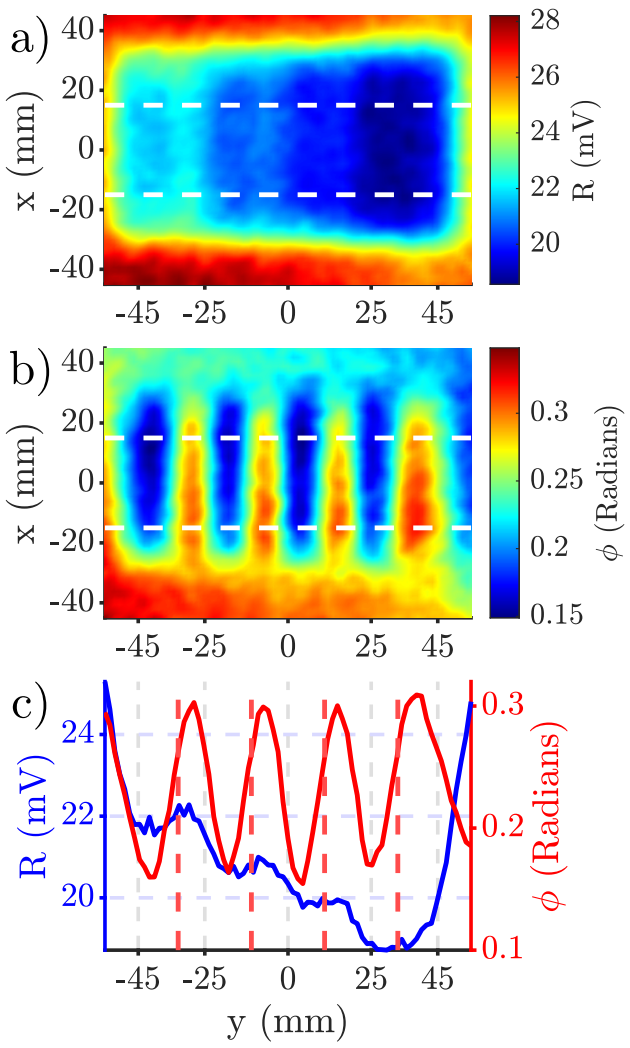

Fig. 4. Experimental results for electromagnetic induction imaging of the sample plate as in Fig. 3, but with a 1.5 mm thick rubber sheet between the plate and the sensor. Same parameters as for Fig. 3.

capability in the inspection of pipelines, thus allowing a complete assessment of their integrity. The combination of EMI-AMs with machine learning techniques [19] would then lead to a transformative approach to efficient corrosion under insulation imaging.

The presented technology is of direct impact to the Oil & Gas Industry.

References

[1] M. Twomey, "Inspection techniques for detecting corrosion under insulation", Mater. Eval. 55, 2, 129-132, Feb 1997.

[2] F. De Vogelaere, "Corrosion Under Insulation", Process Safety Progress 28, 30 – 35, March 2009.

[3] Q. Cao, T. Pojtanabuntoeng, M. Esmaily, S. Thomas, M. Brameld, A. Amer, N. Birbilis, "A Review of Corrosion under Insulation: A Critical Issue in the Oil and Gas Industry", Metals 12, 561-1–561-4, 2022.

[4] P. Bevington, R. Gartman, W. Chalupczak, C. Deans, L. Marmugi, and F. Renzoni, "Non-Destructive Structural Imaging of Steelwork with Atomic Magnetometers", Appl. Phys. Lett. 113, 063503-1–063503-4, August 2018.

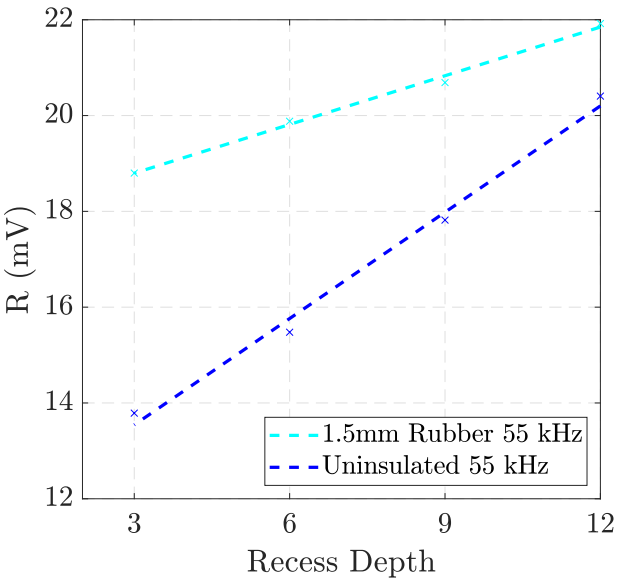

Fig. 5. Amplitude R of the LIA signal amplitude at the center of the different recesses. The two different sets of measurements, and the best linear fit lines, correspond to the case of with/without insulation.

[5] A. Wickenbrock, F. Tricot, and F. Renzoni, "Magnetic induction measurements using an all-optical 87Rb atomic magnetometer", Appl. Phys. Lett. 103, 243503, 2013.

[6] A. Wickenbrock, S. Jurgilas, A. Dow, L. Marmugi, F. Renzoni, "Magnetic induction tomography using an all-optical ^{87}Rb atomic magnetometer," Opt. Lett. 39, 6367–6370, November 2014.

[7] L. Marmugi, and F. Renzoni, "Electromagnetic Induction Imaging with Atomic Magnetometers: Progress and Perspectives", Appl. Sci. 10, 6370, September 2020.

[8] H. Griffiths, "Magnetic induction tomography", Meas. Sci. Technol. 12, 1126, 2001.

[9] L. Wang, "Electromagnetic Induction Imaging: Theory and Biomedical Applications", ASME Press, 2019.

[10] C. Deans, L. Marmugi, and F. Renzoni, "Through-barrier electromagnetic imaging with an atomic magnetometer", Opt. Express 25, 17911–17917, 2017.

[11] I. M. Savukov, S. Seltzer, M. Romalis, and K. Sauer, "Tunable atomic magnetometer for detection of radio-frequency magnetic fields," Phys. Rev. Lett. 95, 063004, 2005.

[12] D. Budker and M. Romalis, "Optical magnetometry," Nat. Phys. 3, 227–234, 2007.

[13] C. Deans, L. Marmugi, S. Hussain, F. Renzoni, "Electromagnetic Induction Imaging with a Radio-Frequency Atomic Magnetometer", Appl. Phys. Lett. 108, 103503, 2016.

[14] A. Wickenbrock, N. Leefer, J. W. Blanchard, and D. Budker, "Eddy current imaging with an atomic radio-frequency magnetometer", Appl. Phys. Lett. 108, 183507, 2016.

[15] C. Deans, Y. Cohen, H. Yao, B. Maddox, A. Vigilante, and F. Renzoni, "Electromagnetic induction imaging with a scanning radio frequency atomic magnetometer," Appl. Phys. Lett., vol. 119, pp. 014001-1–014001-5, July 2021.

[16] B. Maddox, Y. Cohen, and F. Renzoni, "Through-Skin Pilot-Hole Detection and Localisation with a Mechanically-Translatable Atomic Magnetometer," Appl. Phys. Lett., vol. 120, 014002-1–014002-5, January 2022.

[17] L. Marmugi, C. Deans, and F. Renzoni, "Electromagnetic induction imaging with atomic magnetometers: unlocking the low-conductivity regime", Appl. Phys. Lett. 115, 083503-1 –083503-5, August 2019.

[18] C. Deans, L. Marmugi, and F. Renzoni, "Sub-Sm^{-1} electromagnetic induction imaging with an unshielded atomic magnetometer", Appl. Phys. Lett. 116, 133501-1–133501-5, March 2020.

[19] C. Deans, L. D. Griffin, L. Marmugi, and F. Renzoni, “Machine learning based localization and classification with atomic magnetometers”, Phys. Rev. Lett. 120, 033204-1– 033204-5, 2018.